A Study on the Performance of Hydrofoils with Thick Trailing Edges

by

Richard Warren Kimball

Submitted to the Department of Ocean Engineering
in partial fulfillment of the requirements for the degree of

Master of Science in Ocean Engineering

at the

MASSACHUSETTS INSTITUTE OF TECHNOLOGY

September 1997

Author .....
Department of Ocean Engineering
August 8, 1997

Certified by .....
Justin E. Kerwin
Professor of Naval Architecture
Thesis Supervisor

Accepted by .....
J. Kim Vandiver
Chairman, Department Committee on Graduate Students

A Study on the Performance of Hydrofoils with Thick Trailing Edges

by

Richard Warren Kimball

Submitted to the Department of Ocean Engineering
on August 8, 1997, in partial fulfillment of the
requirements for the degree of
Master of Science in Ocean Engineering

Abstract

This thesis documents the measured performance of various 2-D foil geometries with thick trailing edges and compares their performance to the equivalent thin trailing edge foil (called the parent foil). It is postulated that thick trailing edge geometries have better cavitation performance than thin trailing edge geometries due to the effective decrease in surface curvature of the foil. However, there is generally a drag penalty associated with thick trailing edge foils. This study documents lift, drag and cavitation performance of various thick trailing edge geometries and compares them to the "parent" or thin trailing edge geometry. The results indeed show a measurable improvement in cavitation performance with little change in lift performance for the thick trailing edge foils. Though the drag for unaltered thick trailing edge geometries was substantially higher than the "parent" foil, a thick trailing edge geometry with a splitter plate showed drag performance approaching the original parent foil. The foil geometries were derivatives of those developed by Shen and Eppler [5]). Documentation of this work is also provided in References [9] and [3], but this thesis provides much more detail on the study than either of these references.

Thesis Supervisor: Justin E. Kerwin
Title: Professor of Naval Architecture

Acknowledgments

The author would like to thank Dianne Egnor for her tremendous support and efforts regarding the data collection and data reduction for this study. Also, special thanks to Prof. Justin E. Kerwin for his support, encouragement and patience throughout the project. Dr. Charles Mazel provided greatly appreciated advice on the operations of the experimental equipment as well as invaluable access to the high speed video equipment used for the insightful flow visualization. This video equipment was provided by MIT's Edgarton Center. Also the author would like to thank Dr. Bruce Cox for the opportunity to work on the project.

This work was partially funded by Hydrodynamics Research Associates (HRA) directed by Dr. Bruce Cox. HRA funding was provided by the U.S. Navy SBIR Program, Topic No. N90-133 Contract N00024-95-C-4021, NAVSEA CODES 03R5 and 03Z51, technically administered by Mr. C.R. Crockett and Mr. W.G. Berberich.

Additional funding for this project was provided by the U. S. Navy Augmentation Award for Science and Engineering Research Training program (AASERT) under ONR Grant No. N00014-95-1-1240 (MIT OSP No. 63815).

Contents

List of Figures

List of Tables

Chapter 1

Introduction

1.1 Summary

This thesis expands upon the information presented in [9] put into the form of a thesis, and documents an experimental study conducted on advanced 2-D hydrofoil sections with thick trailing edges. A thin trailing edge foil (called the parent foil) was constructed along with thick trailing variants of this foil. It is hypothesized that the thick trailing edge foils will improve the cavitation free performance of the hydrofoil.

The base or parent foil geometry is similar to foil shapes originally developed by Shen and Eppler [5]. The Shen-Eppler type foils have fairly constant pressure distributions over the foil surface, and exhibit desirable cavitation performance, showing less sensitivity to angle of attack when compared to conventional foil geometries (see Ref [10]). Subsequent foil geometries were derivatives of the parent geometry with modifications to the trailing edge shapes incorporating thicker trailing edge shapes. Square, beveled and splitter plate type trailing edge shapes (see Fig. 2-2) were examined and compared to the parent foil geometry (with thin trailing edge).

The experiments were conducted in MIT's variable pressure water tunnel. The following parameters were measured or computed from measured data:

- At various Reynolds numbers (fully wetted conditions):
  - Lift and Drag Coefficient vs. Angle of attack
  - Wake velocity profiles vs. downstream position at design angle of attack
  - Base pressure for selected foils vs. Angle of attack
- At Constant Reynolds number ($\mathrm{Re} \approx 3 \times 10^6$)
  - Cavitation number vs. Angle of attack

In summary the following results were documented:

- The lift performance as a function of angle of attack for the parent, square trailing edge and splitter plate trailing edge foil shapes was essentially the same.

- The cavitation performance of the thicker trailing edge foils showed a wider range of cavitation free operation, as compared to the parent foil
- The drag of the square and beveled trailing edge foils was substantially higher than the parent foil (about 35-40% higher).
- Using a splitter plate trailing edge on the thick trailing edge foil substantially reduced the drag, approaching the parent foil in drag performance (about 6% higher).

Additional documentation on this work along with further information about the foil design procedures can be found in [3]. This work was done under contract from Hydrodynamics Research Associates, (HRA), who also designed and provided the foil sections used in the test.

1.2 Background

The blade sections of propellers operating in the presence of a ship typically see large variations in the inflow conditions. These variations can be caused by the localized inflow effects of the ship wake or could be simply off design operations of the ship itself. Therfore, though a propeller blade section is optimized for one particular operating condition, it is important to consider the performance of the section throughout the typical "off-design" conditions. Though the propellers blade geometric parameters such as pitch, chord, skew etc. are optimized by the designer, the blade section profile, with it's associated thickness and camber distribution was typically selected from a family of shapes (such as those documented by NACA [1]). Sections profiles such as NACA a=0.8 meanline distributions and NACA 66 series was a popular choice for marine propellers, because it exhibited good cavitation characteristics. However, these shapes were originally developed for aeronautical applications and thus were not necessarily ideal for the special problem of cavitation encountered in marine applications.

Cavitation occurs when the local pressure drops below the fluid vapor pressure. By the very nature of lifting surfaces, low pressure regions occur on the foil surface which at sufficiently high loads will eventually cavitate. The major problem encountered with cavitation is it's violent nature, and upon the collapse of these vapor "cavities" a small implosion occurs. These implosions can generate tremendous noise and can be violent enough to damage the blade sections, causing accelerated erosion of the blade surface. As well, the presence of the cavities often changes the performance of the blade section unfavorably. For severe cavitation of a propeller under heavy load, the propeller can become substantially enveloped in cavitation causing thrust breakdown of the propeller (loss of thrust). Hence, designing propellers which operate free of cavitation over a wide operating range is a desirable goal of the propeller designer.

To characterize the cavitation performance of a blade section one typically normalizes the lift force of the section and the global static operating pressure using the following non-dimensional formulas:

For Lift (lift coefficient):

$$C_l = \frac{LiftForce}{\frac{1}{2}\rho V^2 C} \tag{1.1}$$

And for Cavitation (cavitation number σ) :

$$\sigma = \frac{P_{Static} - P_{Vapor}}{\frac{1}{2}\rho V^2} \tag{1.2}$$

Figure 1-1 shows a typical cavitation bucket diagram for a blade section profile (2-D). The line shows the operating conditions where cavitation first occurs (inception). Inside of this "bucket", the foil section operates cavitation free and outside of the bucket cavitation occurs on the blade. Note that a region occurs where the bucket is relatively deep and flat. This is the desirable operating region for the foil section since it can operate at higher speeds (hence lower σ) without cavitating. For superior off design performance one wants the flat region to be as wide as possible to accomodate larger load variations and remain cavitation free.

Recent work by Shen and Eppler [4] and [5] have shown that improvements in cavitation performance of blade sections can be achieved by blade sections which have "roof-top" pressure distributions. Their procedure unloaded the leading edge portion of the foil, shifting the load toward the aft part of the foil while maintaining adequate margin against turbulent separation. The maximum thickness of these sections is well forward of the foil midchord and the leading edge is substantially fuller when compared to conventional sections. Measured improvements in cavitation performance were noted in Reference [10] and several propellers have been tested with success in model scale.

It was postulated that the addition of thick or blunt trailing edges to the profiles of the type previously described would further enhance their cavitation performance. Numerical analysis of these sections showed a significant increase in the width of the cavitation free zone. The effect of the thick trailing edge seems to be related to the fullness of the aft portion of the foil. This was expected to delay both back bubble cavitation (effecting the depth of the cavitation bucket) as well as delaying leading edge sheet cavitation (which should widen the cavitation bucket). Though

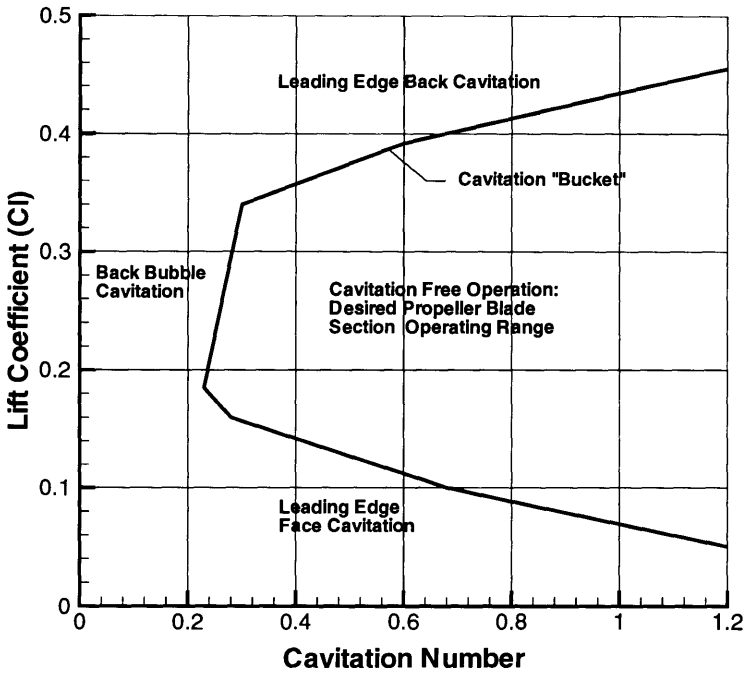

Figure 1-1: Typical Cavitation Bucket Diagram

thick trailing edges may suffer from increased form drag and possibly higher trailing edge noise generation, this study focuses on documenting the effects of trailing edge thickness on cavitation performance.

Chapter 2

Experimental Technique

2.1 Foil Hardware and Setup

2.1.1 Foil Configurations Tested

The general foil shape for the parent foil is shown in figure 2-1. Figure 2-2 shows the various trailing edge sections of the foils tested. The parent foil had a thin trailing edge and all others were thick trailing edge foils. For reference, the thickness of the trailing edge for the thick trailing edge foil was 8mm and the foil chordlength for all foils was 405mm. Note that the beveled trailing edge is a "chopped" version of the square trailing edge. On the thick trailing edge configurations, a single foil was used and the trailing edge sections were removable pieces which were changed in the course of the experiment. The offsets for the parent foil is included in appendix D.

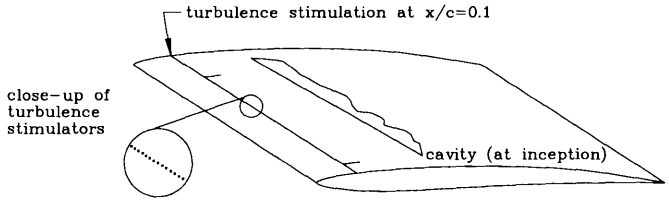

Figure 2-1: Foil schematic showing placement of turbulence stimulation and cavitation locations

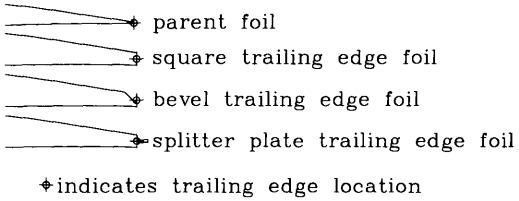

Figure 2-2: Schematic showing the various trailing edge geometries, as well as the trailing edge location used in determining the angle of attack.

Turbulence Stimulation Figure 2-1 shows the foil turbulence stimulation. All foils had turbulence stimulation at $x/c = 0.1$ on both sides. Turbulence stimulation was achieved by a row of cylindrical epoxy dots stretching across the entire span. The epoxy dots are 0.2032mm in height, so they were placed where the boundary layer was expected to be about this thickness. The dots are about 1.25mm in diameter. An estimation of the upper limit of additional form drag due to their presence estimated their drag to be, at most, 6% of the total foil drag. This limit was calculated by assuming the stimulators were 2D cylinders in the free stream. Since they are in the boundary layer and not in the free stream, we expect their drag is over-estimated by this calculation.

2.1.2 Foil Setup

Figure 2-3 shows the foil configuration from the laser table side. The foil is in pressure side up to prevent the tiller mechanism from blocking the laser beams. Figure 2-5 shows the tiller mechanism used to set the angle of attack. Angle of attack was measured using the LDV laser beams and the LDV traverse. With the beam crossing point fixed on either the leading or trailing edge midchord, the traverse-measured positions of the leading and trailing edges can be used to compute foil angle. This method was found repeatable to $\pm$ 0.01 degrees. The traverse/position measurement has a resolution of better than 0.001mm.

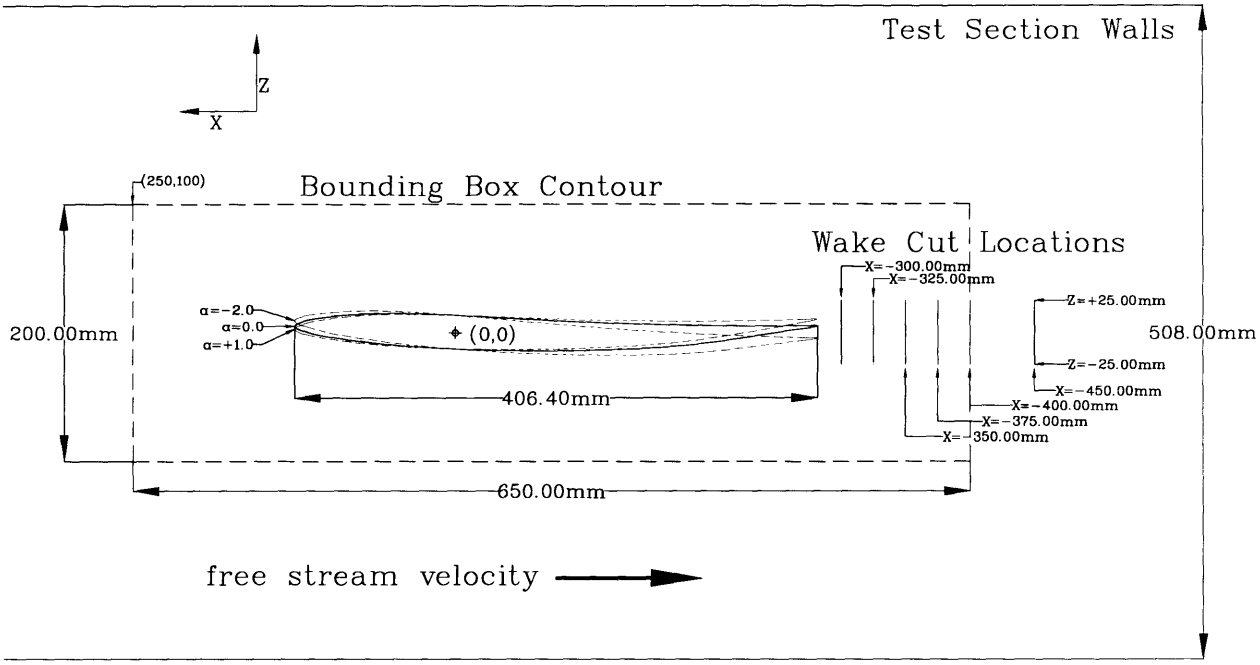

Figure 2-3: The Test Section showing the parent foil and data collection locations

2.2 Tunnel and Test Equipment

2.2.1 MIT Water Tunnel

Figure 2-4 shows MIT's Variable Pressure Water Tunnel. It is approximately 6m by 6m. The square test section (0.508m by 0.508m) is 1.47m in length. Inflow velocity (up to about 8 m/s in the test section) is controlled by a variable speed impeller located in the lower horizontal section of the tunnel. The tunnel pressure can be varied between atmospheric pressure and 5 kPa. Test section static pressure was measured by two ports at the test section mid-height (see figure 2-5). These represent the average tunnel test section pressure and was the reference pressure used for cavitation inception experiments).

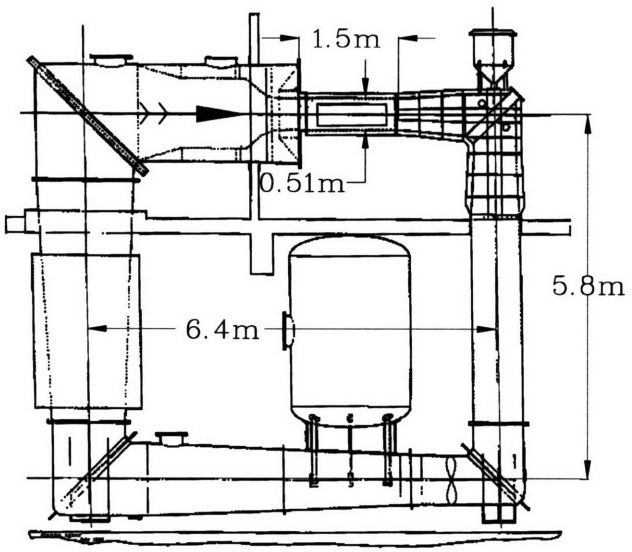

Figure 2-4: The MIT variable pressure water tunnel

2.2.2 Equipment Calibration

Summarized below are the measurement uncertainties for the various measurements used in the experiment. Detailed description of the calibration procedures and calculations appear in appendix C. Fluid properties such as ρ and μ were computed via standard regression formulas based on fluid temperature (see appendix B). For the integrated quantities of Cl and Cd only repeatability values are computed, but this is expected to be much larger than the uncertainty values of individual measurements.

- Measured Quantities:
  - Tunnel Speed (u_∞) : $\pm 0.05 m/s$
  - Tunnel Static Pressure: $\pm 70 Pa$

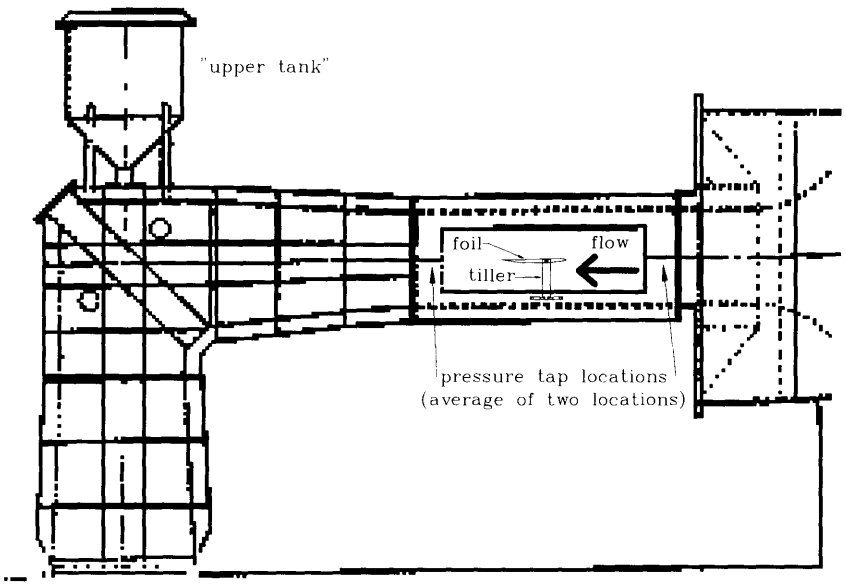

Figure 2-5: The test quadrant of the tunnel, view from the back side, showing the tiller mechanism used to set the angle of attack.

  - Field Point Velocity (Laser): $\pm 0.6\%$ of rdg
    Crosstalk: less than$\pm 0.1\%$ of cross component rdg.
  - Tunnel Water Temperature: $\pm 0.25C$
  - Laser Position: better than $\pm 0.01mm$
  - Foil Angle of Attack: $\pm 0.01^o$

- Computed Quantities:
  - Reynold's Number : $\pm 5\%$
  - Cavitation number at inception: Observation RR: ± 0.05
  - Cavitation number: Calculation Uncertainty: less than $\pm 3.3\%$
  - Lift Coefficient by Contour Integration (RR) : less than ± 0.0065
  - Drag Coefficient by Contour Integration (RR) : less than ± 0.001

2.2.3 Tunnel Effects on Measurements

Tunnel Free Stream Turbulence Free stream turbulence intensity as a function of tunnel speed was measured previously in an empty tunnel by Lurie [7] using hot wire annemometry. These measurements showed a free stream turbulence intensity of 1% or less.

Tunnel Air Content (for cavitation measurements) Tunnel air content during cavitation experiments was estimated using a global air tunnel air volume measurement technique. Just prior to the cavitation experiments the still water tunnel height was measured at two different pressures. The rise in height due to the lower pressure was assumed to be due to the expansion of the undissolved air in the tunnel. This height was converted into a volume change using the tunnels upper tank geometry. Using the ideal gas equation an estimate of the tunnel air volume at any test pressure. The percentage air content was then computed from the ratio of undissolved tunnel air at test condition divided by the total tunnel water volume. This method gives a rather crude estimate of tunnel air content for it does not take into account the hydrostatic depth effects on the air volume. During experiments the tunnel air content was always measured less than 1% by volume.

Upper and Lower Tunnel Wall Boundary Layers Boundary layer growth on the walls above and below the foil was studied for the possible cambering of the flow field due to asymmetric growth on the upper and lower walls. We measured each wall's boundary layer profile for the parent foil at the design angle of attack ($\alpha \approx -0.5^{o}$). As well, a Navier-Stokes RANS code, DTNS2D, was run with the parent foil geometry including upper and lower tunnel walls and numerically calculated boundary layer profiles was generated at the measurement locations. Figures 2-6 and 2-7 show good agreement between measurement and computation. The results showed a small net "cambering" of the flow which could affect lift. This "cambering" phenomenon should not effect drag greatly.

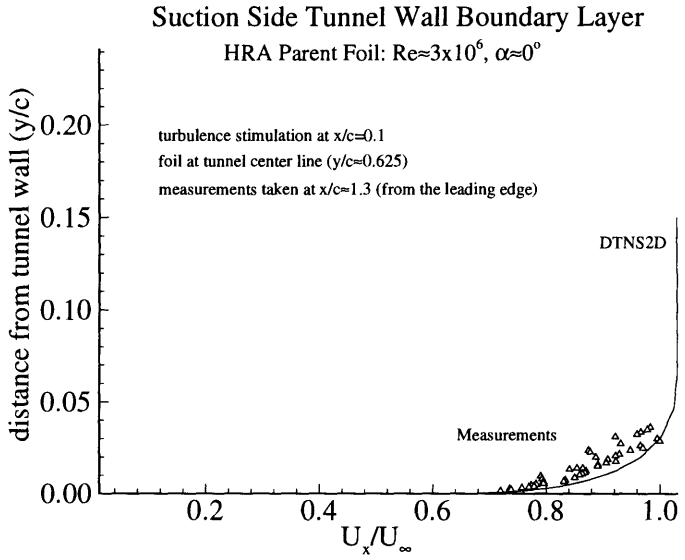

Figure 2-6: The window boundary layer on the suction side

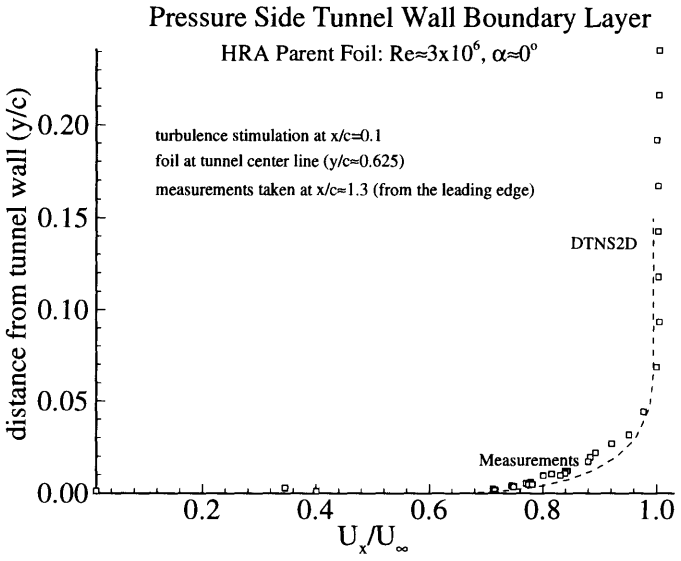

Figure 2-7: The window boundary layer on the pressure side

Side Wall Boundary Layers The side wall boundary layers also had some measured effect on the foils' performance. The side wall boundary layer growth effectively accelerated the mean interior flow. This manifested into a net mass flux increase out of the closed loop integration contour in our force calculation routine. The integrated lift forces were corrected by this added momentum to give 2D lift (to be discussed later). The magnitude of this mass flux defect was about 2-4% of the mass flux through the inflow side of the measurement contour.

2.3 Experimental Procedures

2.3.1 Cavitation Buckets

The cavitation inception study consists of the following steps:

1. Set foil angle of attack (roughly)
2. Bring tunnel up to desired speed (U_∞)
3. Lower pressure until cavitation is visible
4. Determine angle by measuring leading and trailing edge position with laser crossing

To determine cavitation inception, the foil was lit with a focused beam of light. In a dark room, a cavitation bubble will reflect strongly, visible against the matte black surface of the foil. By our definition, "inception" occurs when the cavitation

bubble spreads across more than 3/4 the span of the foil (see Fig. 2-1). The turbulence stimulators would often locally cavitate much earlier than our "inception" observation, but was ignored until the cavitation formed a single sheet on the foil. This was justified since a full scale foil would not have these stimulators present.

For the square and bevel removable trailing edge foils, the pressure was brought up to 50 kPa and brought down again to inception pressure three or more times, in order to get a repeatability range on our judgment of inception, and these repeatability ranges are shown as error bars on the cavitation bucket diagrams.

2.3.2 Lift and Drag by Contour Method

The method used to determine the foil lift and drag coefficients was originally developed by Kinnas [6]. The method consists of measuring horizontal and vertical velocities along a constant span contour and integration around the contour to find net forces on the foil. Both momentum and local pressure must be integrated and added to find the net force.

The method assumes the following:

- Incompressible flow
- The measurement contour is essentially in a potential flow region (not true in the foil wake, but this region is treated specially as described later)
- 2-D flow (small spanwise variations)

The method first computes the mass flux through the contour. Though this should be zero, we always measure a net positive flux out of the contour. We believe this is due to side wall boundary layer growth on the tunnel. For a first order correction, the momentum from this added flux must be subtracted from the net horizontal forces to correct for this 3-D effect. However, since the magnitude of this additional flux momentum is on the order of the drag measurement, the uncertainty in drag measurements using this method are high. Thus an alternative "local" method was used to determine the drag coefficient. This method consisted of computing the momentum deficit in the wake region only (see Fig.2-8). The reference for computing the defect was determined by fitting a quadratic curve to the velocity profiles in the upper and lower outer flow regions (i.e. outside of the wake). This was considered to approximate the flow if the viscous wake were not present. The wake defect velocity at each wake point was the difference between this interpolated line and the measured velocity at that corresponding position.

The contour used for all the foil force measurements was a rectangular box as shown in Figure 2-3. The flow was measured to be insensitive to spanwise position for at least the middle 80% of the foil span. For reasons of laser data collection, the spanwise position of the contour was at 1/3 span into the tunnel.

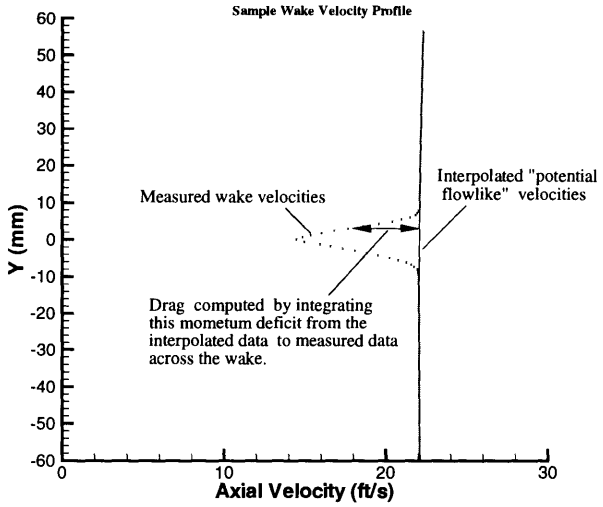

Figure 2-8: Contour Wake Velocity Profiles showing wake interpolation for momentum deficit drag computation

2.3.3 Other Measurements

Wake velocity profiles were measured for the parent, square trailing edge, bevel trailing edge, and splitter plate trailing edge foils. All wake cuts were done at $\alpha \approx -0.5^o$ and at two Reynolds numbers (Re $\approx 1 \times 10^6$ and Re $\approx 3 \times 10^6$). In general, velocity profiles were taken at $x/c \approx 0.05$, 0.11, 0.17, 0.23, 0.29, 0.42 (from the trailing edge), and z/c locations of 80 points between 0.05 above and 0.07 below the trailing edge (see Fig. 2-3).

For some of the thick trailing edge foils an averaged trailing edge base static pressure was measured at the trailing edge midchord point. This was done using a liquid-liquid manometer where one liquid was water and the other liquid was Meriam "blue juice" with a specific gravity of 1.75 at standard atmospheric temperature and pressure..

Chapter 3

Discussion of Results

3.1 Cavitation Inception

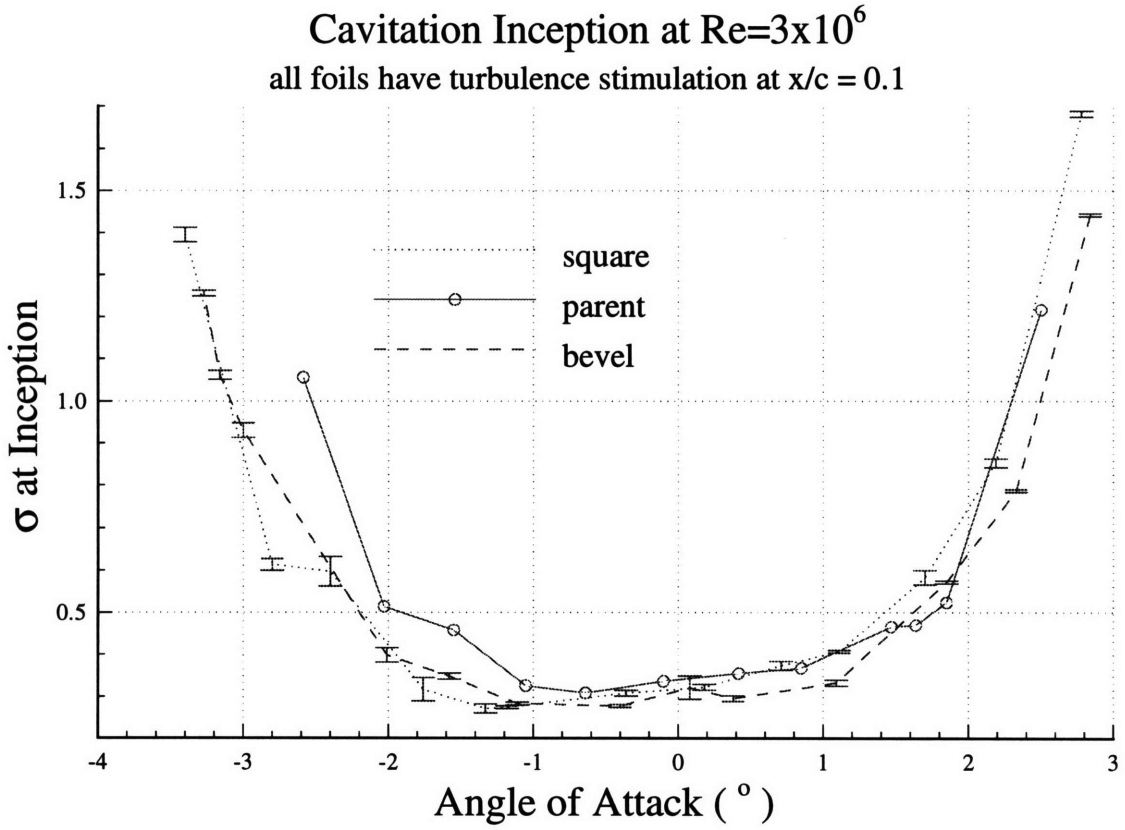

Figure 3-1: Cavitation Inception vs. Angle of Attack

The cavitation performance of the various test foils is shown in figures 3-1 and 3-2. Figure 3-1 is the data as measured, showing cavitation number vs. angle of attack. Figure 3-2 shows the cavitation number plotted against lift coefficient. The lift coefficients were computed from the fully wetted lift vs. α linear regressions from

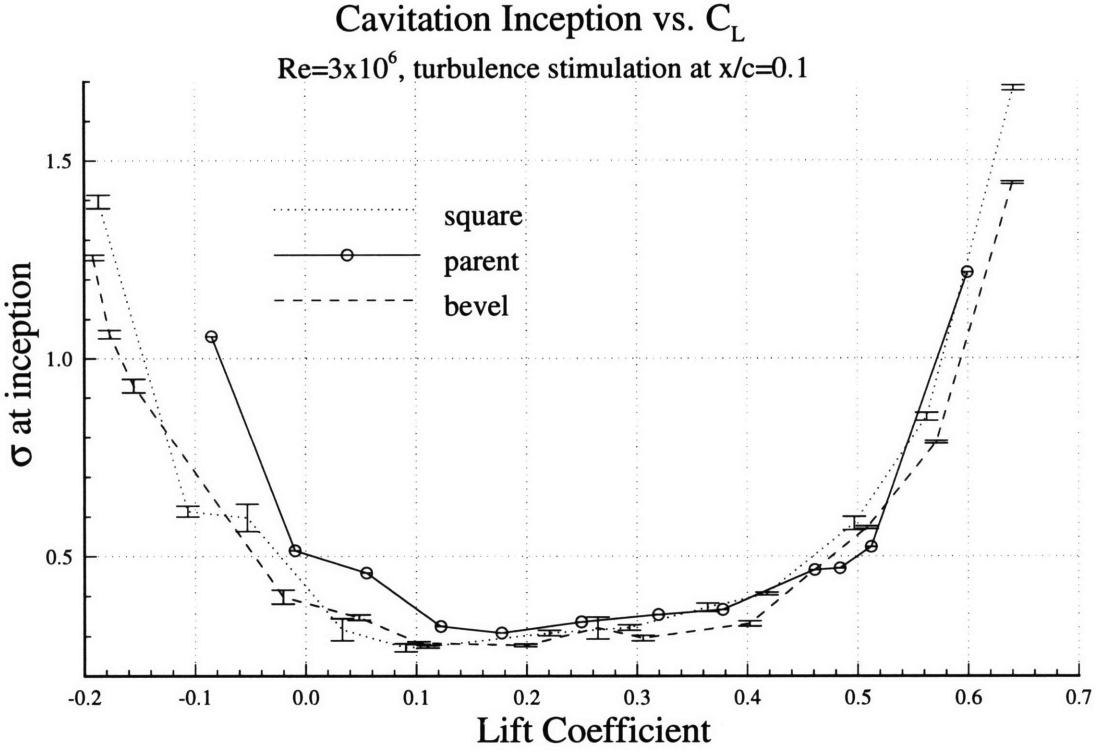

Figure 3-2: Cavitation Inception vs. C_L

the bounding box results.

Figures 3-1 and 3-2 show that the cavitation performance of the thicker trailing edge foils has a wider range of cavitation free performance as compared to the parent foil. As well, the lower bound of the buckets is lower for the thick trailing edge foils as expected. This indicates that the expected reductions of back bubble cavitation and leading edge face cavitation have been achieved. Data tables for the measured data can be found in appendix A.

3.2 Lift and Drag Performance

Lift and Drag coefficients were computed for the various foils at various angles and Reynolds numbers. The results are shown in Figs. 3-3 - 3-8.

3.2.1 Parent Foil Results

One curious but consistent behavior was the variation in C_L due to Reynolds number (see Fig. 3-3). In all cases the lowest Reynolds number condition showed higher lift coefficient than the higher Reynolds number condition. Typically, for conventional foils, we expect an increase in C_L for increases in Reynolds number due to a thinning of the boundary layer.

Figure 3-4 shows C_L and C_D as a function of angle of attack for the Parent foil. Curves are shown for various Reynolds numbers.

3.2.2 Performance comparisons of various Thick Trailing Edge foils

Figures 3-5, 3-6, and 3-7 show the C_L and C_D performance of the various thick trailing edge foils tested. Figure 3-8 shows C_L and C_D for all the foils at $Re \approx 3 \times 10^6$, including the parent foil. For the parent foil the slope of the lift curve is 0.135 and it's zero lift intercept is at -1.97 degrees. The square trailing edge foil has a lift slope of 0.136 and a zero lift intercept of -1.95 degrees. The beveled trailing edge foil showed some offset in the C_L vs. α curve, (zero-intercept of -1.79 degrees possibly due to the change in effective camber of the foil due to the bevel. However, The bevel edge foil lift slope was almost identical to the other foils (lift slope = 0.135).

The most interesting comparison is that of the drag coefficients for these foils as compared to the parent foil. Figure 3-8 shows the C_D vs. α for all four foils. Note that the square trailing edge foil and the bevel trailing edge foil had quite high drag, while the splitter plate trailing edge foil had drag performance approaching that of the parent foil. This result is significant and shows that trailing edge detail can have a quite large effect on foil drag.

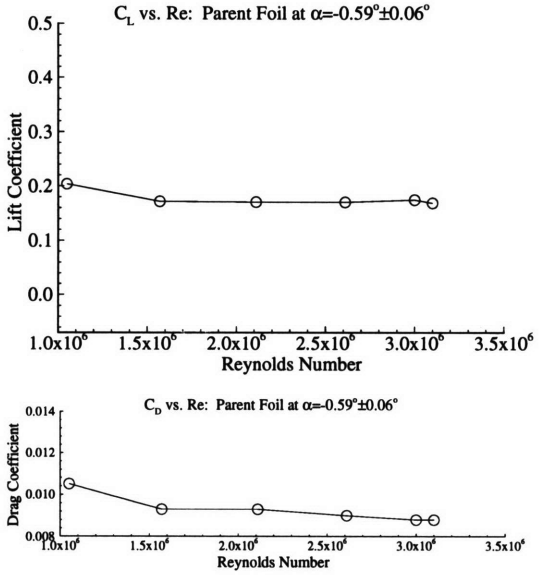

Figure 3-3: C_L vs. Re, C_D vs. Re for the Parent Foil at $\alpha \approx -0.5^o$

3.3 Other Measurements and Observations

Wake Velocity Profiles Figure 3-9 shows the wake velocity profiles as a function of position behind the foil. Comparing the wake of the parent foil to that of the square

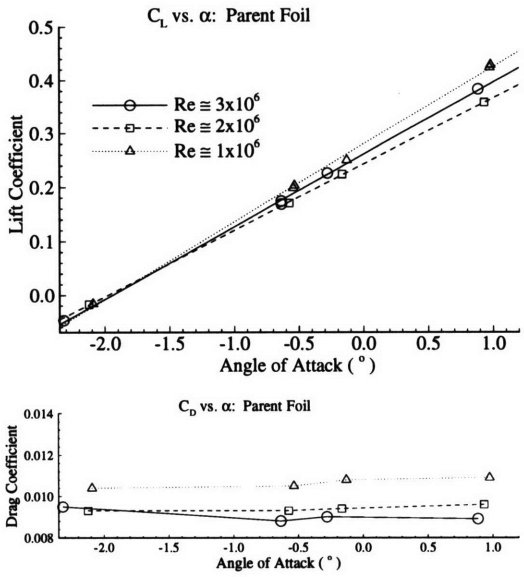

Figure 3-4: C_L vs. α, C_D vs. α for the Parent Foil at Re $\approx 1 \times 10^6$,2×10^6, and 3×10^6

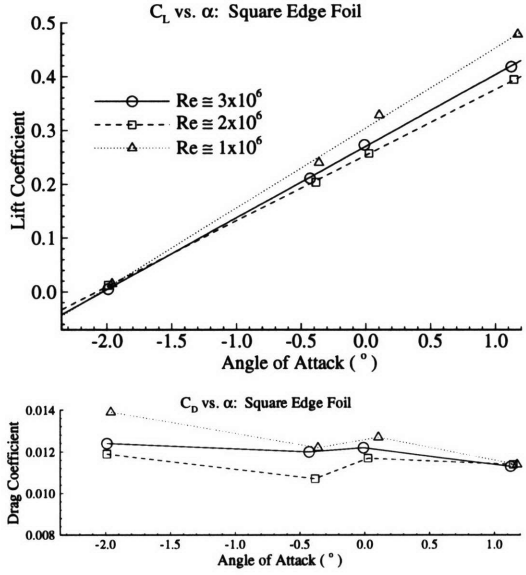

Figure 3-5: C_L vs. α, C_D vs. α for the Square Edge Foil at Re $\approx 1 \times 10^6$,2×10^6, and 3×10^6

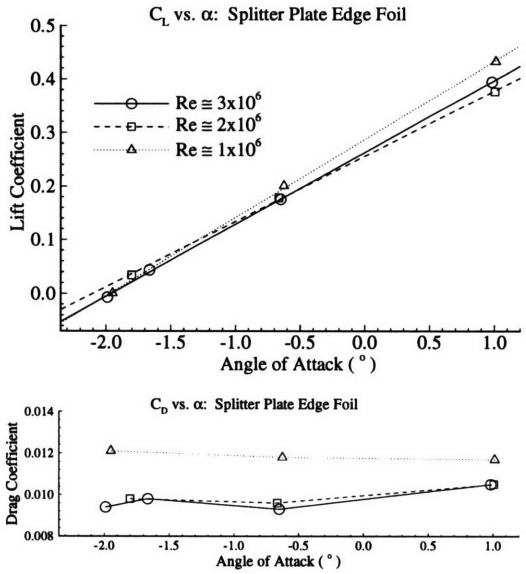

Figure 3-6: C_L vs. α, C_D vs. α for the Splitter Plated Edge Foil at Re $\approx 1 \times 10^6$,2×10^6, and 3×10^6

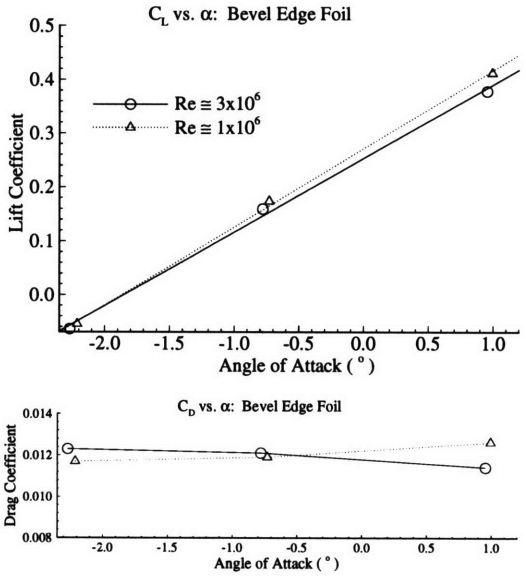

Figure 3-7: C_L vs. α, C_D vs. α for the bevel Edge Foil at Re $\approx 1 \times 10^6$ and 3×10^6

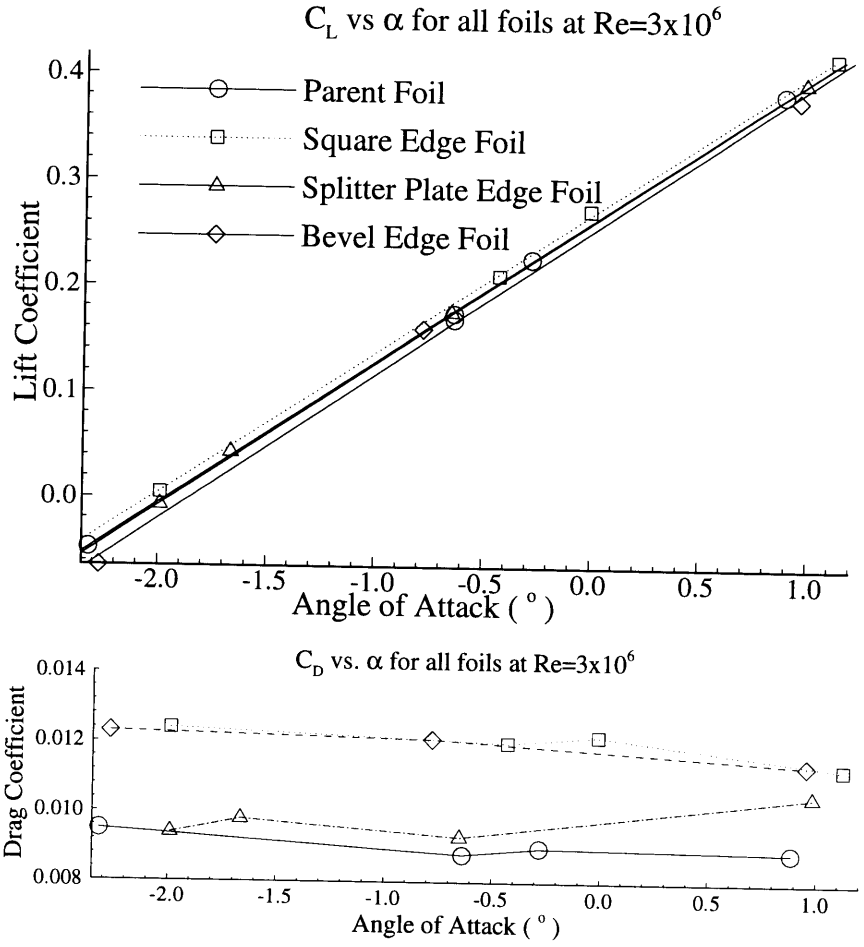

Figure 3-8: C_L vs. α, C_D vs. α for all foils at Re $\approx 3 \times 10^6$

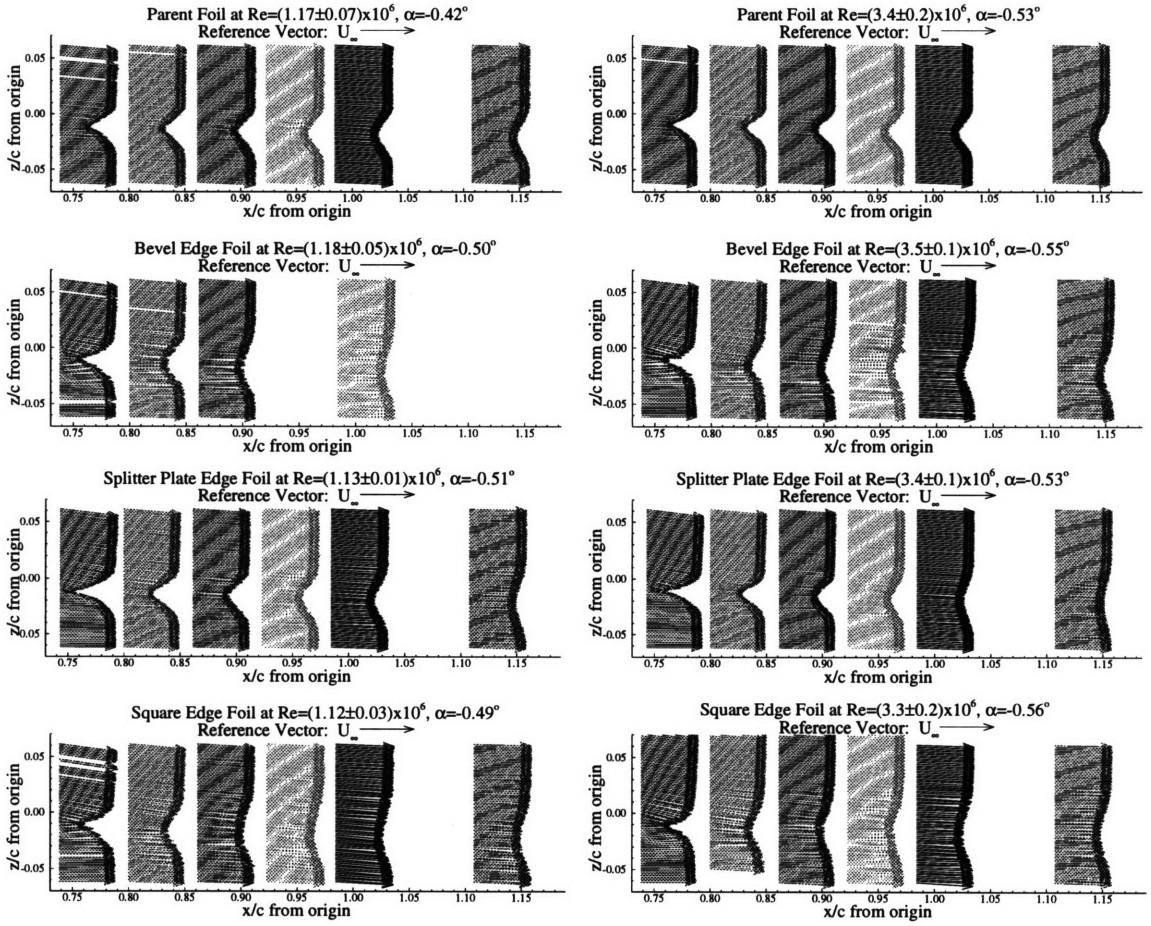

Figure 3-9: Wake Velocity Profiles for All Foils at $\alpha \approx -0.5^o$, Re $\approx 1\text{x}10^6, 3\text{x}10^6$. Re ranges represent the drift in the course of the experiment. α drifted less than $\pm 0.01^o$ in all experiments. Positive z/c indicate the suction side of the foils, the trailing edge was located near $x/c = 0.69$, $z/c = -0.01$ from the origin.

and beveled trailing edge, we see the latter foils have significantly thicker wake dents. This is expected, and it follows that these thicker trailing edge foils have higher drag.

Dye Injection Flow Visualization of Unsteady Trailing Edge Flows Figure 3-10 shows the trailing edge flow patterns of four foil trailing edge shapes. All cases were photographed at a Reynold's number of $2x10^6$ and an angle of attack of approximately -0.5^o. Dye was injected out of the trailing edge under equivalent conditions for each foil. Notice the strong vortex shedding of the square trailing edge foils. The bevel trailing edge showed showed a strong vortex on the pressure side, but showed a curiously weak shed vortex from the suction side. The strouhal number for these two configurations based on the square trailing edge thickness was 0.23.

The splitter plate configurations showed little vortex shedding behavior. This trailing edge wake flow approaches that of the parent foil trailing edge flow pattern (which was tested but not presented here). These results agree qualitatively with the drag measurements and velocity profiles discussed earlier.

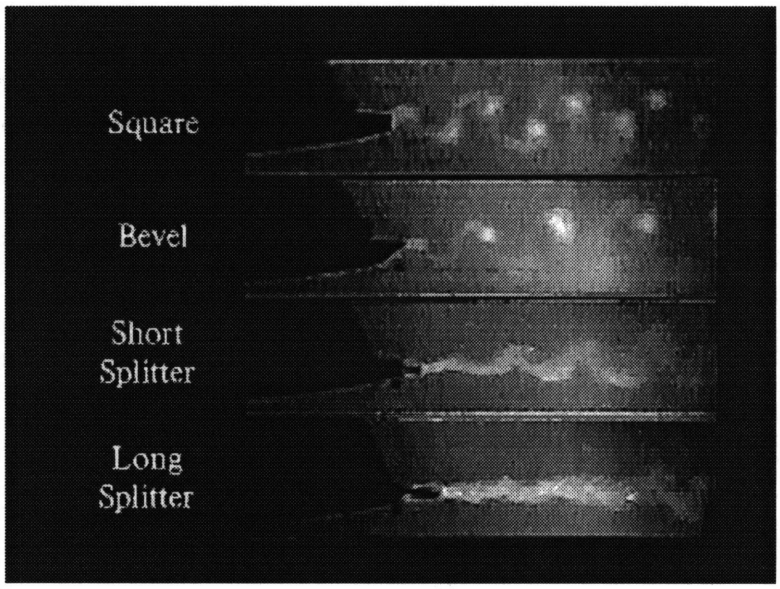

Figure 3-10: Flow visualization of trailing edge flows for trailing edge shapes; *alpha* = 0.5^o, Re=2ee6 (Note Foil suction side is down in this figure)

Trailing Edge Base Pressure Measurements Trailing edge static base pressure was measured for the square and splitter plate trailing edge foils, the former at three Reynolds numbers, the latter at two. Base pressure is a good indicator of foil drag and, as Fig. 3-11 shows, the splitter plate's base pressure was lower than that of the square trailing edge.

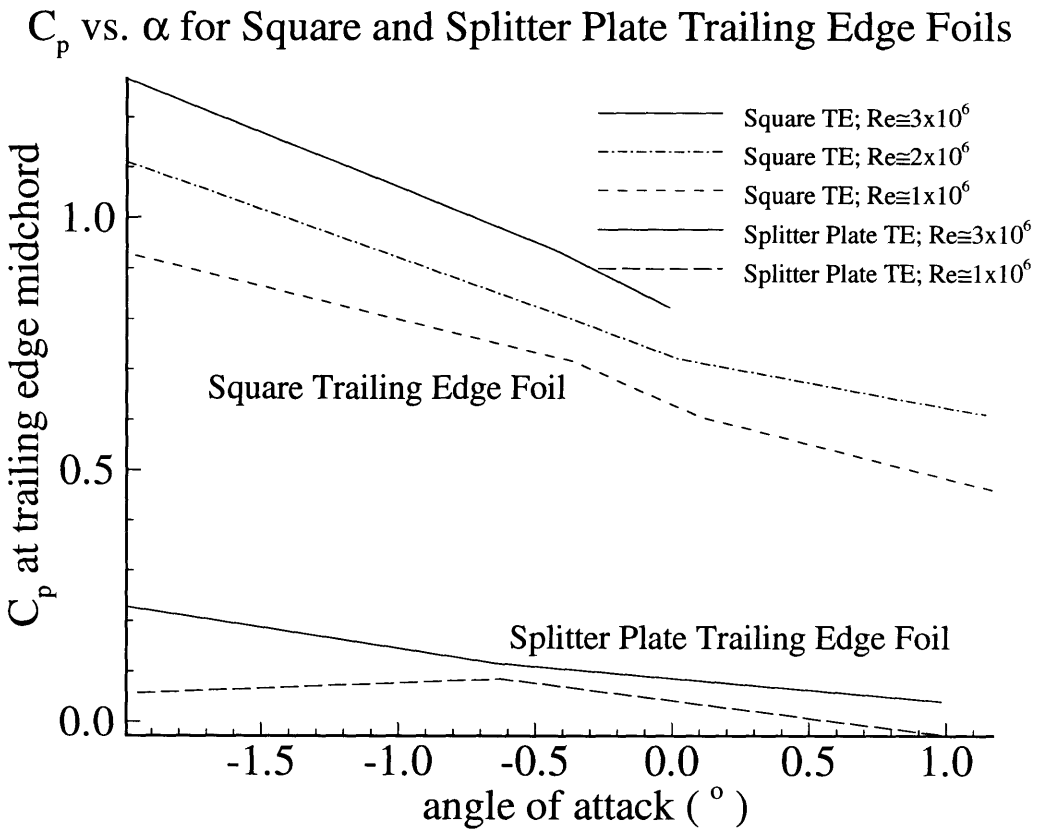

Figure 3-11: C_p vs. α for the square and splitter plate trailing edge foils at various Reynolds numbers

Chapter 4

Conclusions and Recommendations

In summary, the performance of the parent and thick trailing edge foils was measured and behaved mostly as expected. Below are summarized the key results and observations:

- Cavitation Performance
  - The thick trailing edge foils showed measurable improvement in cavitation performance compared to the thin trailing edge parent foil (see figure 3-2)
- Lift Performance
  - The lift vs. angle of attack performance was similar for the various foils tested(figure 3-8). In other words, the addition of thickness to the trailing edge did not significantly alter the lift performance of the foil.
  - The test foils showed unpredicted lift behavior vs. Reynolds number Figure 3-3 shows that the lift of the parent foil decreases Reynold's number is increased.
  - The bevel trailing edge foil exhibited a shift in the $C_l vs \alpha$ curve. This is probably due to the effective camber change in the foil due to the bevel's presence.
- Drag Performance
  - The drag of the thick trailing edge foils (Square and Bevel) was much higher than the parent foil (36% and 38% higher respectively) at design angle of attack.
  - The drag of the splitter plate geometry approached that of the parent foil, showing only 5.7% higher drag than the parent at design angle of attack.
  - Flow visualization showed significant variation in shed vorticity patterns for the various thick trailing edge design. Highly coherent shed vorticity was

observed for the square and bevel trailing edges, whereas very weak shed vorticity was observed for th splitter plate configurations. These observations substantiate the observed behaviors in foil drag measurements.

- Other Observations and Comments
  - Side wall boundary layer effects were observed in the contour force calculation There result is a small 3-D effect to the flow field.
  - The presence of the upper and lower tunnel walls effects the lift performance of the foil due to their image effect as well as their boundary layer growth. These wall effects must be considered in comparisons between numerical and measured results.

As expected, the incorporation of thick sections did measurably improve the cavitation performance over the parent foil with almost no change to lift performance. The drag of the thicker sections was substantially higher for for sections with strong trailing edge vortex shedding. Trailing edge treatments to these thick sections which broke up this vortex shedding showed substantially lower drag, approaching that of the thin parent foil.

An additional consequence of the strong vortex shedding seen in the thick trailing edge sections is the potential for strong acoustic radiation of the section as well as acoustic excitation of the blade (such as blade "singing"). Such acoustic propagation is obviously undesirable in a blade section. This study shows examples of how small trailing edge geometry details can essentially eliminate this vortex structure. With such trailing edge treatments it is clear that the thick trailing edge geometries have promise in improving the cavitation performance of hydrofoil sections for use on propellers and lifting surfaces.

Recommendations It has been shown that thick trailing edges can be successfully introduced to a foil section and increase the cavitation performance of the foil. The next logical step would be to incorporate these thick trailing edge sections to a propeller design and test the propellers cavitation performance. Such a propeller may want to have each blade use a different modification to the blade section for profile. For example, one blade may be use the thin trailing edge section, another use a blunt trailing edge section. The assumption made is that the blade to blade effects are small. The advantage of this type of design would be a direct and comparable observation of the cavitation of each blade section under exactly the same conditions.

Though the thick trailing edge foils were successful at improving the cavitation performance, the measured increased drag of the blunt trailing edge foils is substantial. This study showed that trailing edge treatments such as the addition of a splitter plate significantly reduced the drag problem, this configuration may not be desirable in a production situation. Further research on different trailing edge treatments

could establish a trailing edge treatment which achieves the vortex shedding break-up behavior of the splitter plate, but is more easily incorporated onto a production propeller blade section. In fact, some promising work done by F. S. Archibald [2] indicated that thick trailing edges with concave shapes significantly reduced vortex shedding strength.

Appendix A

Tabulated Data and Results

Tables A.1, A.2, and A.3 show the tabulated bounding box data, bounding box results, and cavitation data, respectively.

foil	U(m/s)	$\alpha(deg)$	$d\alpha(deg)$	$P - P_o(Pa)$	Q(m/s)	T(C)	dT(C)
parent	6.873	-2.318	0.002		-0.0777	23.3	
	6.858	-0.637	0.006		-0.0564	23.6	
	6.864	-0.636	0.006		-0.0518	25.0	0.6
	6.882	-0.28	0.01		-0.0917	25.2	0.7
	6.858	0.885	0.005		-0.0817	26.7	0.8
	5.709	-0.6155	0.0005		-0.0411	25.6	0.6
	5.730	0.925	0.005		-0.0555	25.3	0.3
	4.566	-2.124	0.001		-0.0396	22.8	0.3
	4.547	-0.575	0.008		-0.0378	26.1	0.2
	4.557	-0.1655	0.0004		-0.0607	24.4	0.2
	4.547	0.933	0.001		-0.0588	27.2	
	3.392	-0.551	0.006		-0.0296	26.1	
	3.398	0.96	0.004		-0.0396	25.0	0.2
	2.315	-2.093	0.001		-0.0165	22.8	0.2
	2.278	-0.535	0.002		-0.0204	26.1	0.2
	2.264	-0.543			-0.0201	25.6	
	2.290	-0.13	0.01		-0.0250	24.4	0.2
	2.286	0.975	0.005		-0.0277	25.0	0.2
	2.255	0.982	0.007		-0.0219	25.6	0.2
square	6.861	-1.99	0.03	2.99e+04	-0.0661	27.8	0.6
	6.879	-0.43	0.02	2.21e+04	-0.0735	29.4	1.1
	6.876	-0.01	0.01	1.94e+04	-0.0695	26.1	0.6
	6.885	1.125	0.005		-0.0887	28.9	1.1
	4.541	-1.99	0.01	1.14e+04	-0.0479	28.6	0.3
	4.547	-0.384	0.002	8.26e+03	-0.0494	30.0	0.3
	4.544	0.025	0.005	7.41e+03	-0.0497	26.7	0.2
	4.544	1.145	0.005	6.24e+03	-0.0646	29.7	0.3
	2.246	-1.96	0.02	2.32e+03	-0.0256	28.9	0.2
	2.258	-0.36101	1e-05	1.81e+03	-0.0344	30.0	0.3
	2.249	0.105	0.005	1.53e+03	-0.0247	27.2	0.2
	2.254	1.175	0.005	1.16e+03	-0.0421	30.0	0.2
spl. plate	6.928	-1.99	0.01	5.45e+03	-0.1240	27.8	0.6
	6.888	-1.665	0.005		-0.1039	27.5	
	6.894	-0.65	0.04	2.75e+03	-0.0881	30.0	1.1
	6.861	0.983	0.003	9.45e+02	-0.1128	27.8	0.6
	4.541	-0.665	0.005	7.98e+02	-0.0549	30.6	0.2
	4.553	1.006			-0.0762	28.6	
	2.269	-1.95	0.01	1.45e+02	-0.0411	28.3	0.2
	2.263	-0.625	0.005	2.18e+02	-0.0241	30.6	
	2.261	1.013	0.003	-7.26e+01	-0.0378	28.3	0.2
bevel	6.900	-2.27	0.02		-0.122	28.1	0.3
	6.890	-0.78	0.01		-0.0966	29.4	0.6
	6.887	0.954	0.004		-0.0911	28.3	0.6
	4.453	-0.7492	0.0004		-0.0686	30.0	0.2
	2.268	-2.212	0.004		-0.0357	28.6	0.3
	2.255	-0.730	0.004		-0.0341	30.0	0.2
	2.264	0.994	0.001		-0.0329	28.9	

Table A.1: Bounding Box Data

foil	$Re(\times 10^6)$	α	$C_L(\Gamma)$	$C_L(p)$	C_p	C_D
parent	2.99	-2.318	-0.0463	-0.0474		0.0095
	3.00	-0.637	0.1699	0.1743		0.0088
	3.10	-0.636	0.1652	0.1686		0.0088
	3.12	-0.28	0.2212	0.2265		0.0090
	3.22	0.885	0.3756	0.3836		0.0089
	2.61	-0.6155	0.1658	0.1702		0.0090
	2.60	0.925	0.3578	0.3666		
	1.96	-2.124	-0.0168	-0.0173		0.0093
	2.11	-0.575	0.166	0.1704		0.0093
	2.03	-0.1655	0.2189	0.2244		0.0094
	2.16	0.933	0.3511	0.3587		0.0096
	1.57	-0.551	0.166	0.1716		0.0093
	1.53	0.96	0.3552	0.3658		
	0.996	-2.093	-0.0156	-0.0159		0.0104
	1.05	-0.535	0.1957	0.2035		0.0105
	1.04	-0.543	0.1912	0.1987		
	1.02	-0.13	0.2406	0.2505		0.0108
	1.03	0.975	0.4084	0.4241		0.0109
	1.03	0.982	0.4317	0.4289		
square	3.30	-1.99	0.0048	0.0052	1.2760	0.0124
	3.45	-0.43	0.2065	0.2107	0.93618	0.0120
	3.18	-0.01	0.2656	0.2727	0.82309	0.0122
	3.40	1.125	0.4096	0.4178		0.0113
	2.23	-1.99	0.0118	0.0123	1.11027	0.0119
	2.31	-0.384	0.1989	0.2034	0.80266	0.0107
	2.13	0.025	0.2501	0.2568	0.71998	0.0117
	2.29	1.145	0.385	0.3938	0.60691	0.0114
	1.11	-1.96	0.0136	0.0152	0.92527	0.0139
	1.15	-0.36101	0.229	0.24	0.71455	0.0114
	1.07	0.105	0.3142	0.3279	0.60546	0.0122
	1.15	1.175	0.4562	0.4779	0.45880	0.0127
spl. plate	3.33	-1.99	-0.0072	-0.0072	0.22798	0.0094
	3.29	-1.665	0.042	0.0433		0.0098
	3.50	-0.65	0.1711	0.1753	0.11640	0.0093
	3.30	0.983	0.4063	0.3942	0.04031	0.0105
	2.29	-1.802	0.0336	0.0343		0.0098
	2.34	-0.665	0.1744	0.1784	0.07771	0.0096
	2.24	1.006	0.3663	0.3765		0.0105
	1.11	-1.95	-0.0004	0.0006	0.05666	0.0121
	1.17	-0.625	0.1928	0.2005	0.08539	0.0118
	1.10	1.013	0.4143	0.4322	-0.02854	0.0117
bevel	3.34	-2.27	-0.0624	-0.0642		0.0123
	3.45	-0.78	0.1595	0.1595		0.0121
	3.35	0.954	0.3676	0.3780		0.0114
	2.31	-0.7492	0.1465	0.1508		0.0113
	1.11	-2.212	-0.0534	-0.0550		0.0117
	1.15	-0.730	0.1663	0.1740		0.0119
	1.12	0.994	0.3952	0.4117		0.0126

Table A.2: Bounding Box Results

Blunt 1 bevel te			**Blunt 1 square te**			**parent foil**	
α	σ	$\Delta\sigma$	α	σ	$\Delta\sigma$	α	σ
-2.71	1.26	0.02	-2.84	1.40	0.03	-2.59	1.06
-2.59	1.06	0.02	-2.24	0.61	0.02	-2.03	0.51
-2.43	0.93	0.02	-1.83	0.60	0.03	-1.55	0.46
-1.45	0.40	0.01	-1.19	0.32	0.02	-1.05	0.33
-1.01	0.35	0.01	-0.77	0.27	0.01	-0.64	0.31
-0.54	0.28	0.01	-0.61	0.27	0.01	-0.10	0.34
0.16	0.28	0.02	0.20	0.31	0.01	0.42	0.35
0.65	0.32	0.02	0.74	0.32	0.01	0.85	0.37
0.94	0.30	0.01	1.28	0.37	0.01	1.47	0.47
1.65	0.33	0.01	1.68	0.41	0.01	1.64	0.47
2.42	0.57	0.01	2.27	0.58	0.02	1.85	0.52
2.89	0.79	0.02	2.76	0.85	0.02	2.50	1.23
3.40	1.44	0.02	3.34	1.68	0.02		

Table A.3: Cavitation Inception tabulated data: Blunt 1 foils, at Re $\approx 3 \times 10^6$, with turbulence stimulation at $x/c = 0.1$

Appendix B

Fluid Properties: Curve-fit Formulas

Linearization formulas for the material properties used in the data reduction:

- for the density of water in kg/m^3 (in the temperature range 23C-30C):

$$\rho_w = -0.2644\,T + 1003.582 \tag{B.1}$$

  where T is the water temperature in Celsius degrees.

- for the difference in density of "blue juice" and water in kg/m^3 (in the temperature range 20C-25C):

$$\rho_{bj} - \rho_w = -0.7669\,T + 757.7241 \tag{B.2}$$

  where T is the air temperature of the room (by assumption the temperature of the water and "blue juice" in the manometer) in Celsius degrees.

- kinematic viscosity of water in m^2/s (in the temperature range of 20C-30C):

$$\nu = -2 \times 10^{-8}(T - 20) + 1 \times 10^{-6} \tag{B.3}$$

  where T is the water temperature in Celsius degrees.

- Vaporization Pressure of water in m^2/s (in the temperature range of 20C-30C):

$$P_{vap} = 0.1907 \times T - 1.4746(kPa) \tag{B.4}$$

  where T is the water temperature in Celsius degrees. (Source: linear interpolation of values published in Newman Ref. [8].

Appendix C

Calibration & Uncertainty Analysis

C.1 Methods

Error analysis performed on measured quantities was done using the standard error analysis techniques. The errors are assumed random variables and their effect total effect is approximated by summing the first error term in the Taylor series expansion of the relation used in computing the measured quantities. Estimates of the error range for each variable in the system are estimated from quantities like instrument resolution, repeatability etc. The error analysis performed here, though not rigorous, should provide the reader with reasonable estimates of the error ranges for the data presented.

For some integrated quantities such as lift and drag coefficients, a formal error analysis was not performed. Rather, a reliability and reproduceablity (R & R) analysis was performed to provide a reasonable estimate of the error in the method.

C.2 Measured Quantities

Laser Velocity Calibration To calibrate the laser velocity measurement, we use a "spinning disk", a rotating plane perpendicular to the beam path. The velocity at which a point on the surface is moving can be calculated from the following equation:

$$v = \omega \times r \tag{C.1}$$

where v is the velocity of the measurement point, ω is the rotation rate, and r is the distance between the measurement point and the center of rotation. The accuracy of this calibration is determined by the laser traverse system (r) and a photo-optic rpm sensor circuit and frequency counter (ω). The uncertainty analysis for the LDV velocity shows the uncertainty in velocity is within $\pm 0.6\%$ This method also allows the measurements and correction of beam parallelness to the traverse axes. Cross talk between velocity components was measured to be less than 0.1% of cross component reading.

Tunnel Static Pressure An electronic manometer was used to determine tunnel pressure during the cavitation studies. It was calibrated each day of experimentation against a water column which extended the vertical height of the tunnel. The uncertainty of this method depends chiefly on the accuracy of water column height measurement ($\pm 7mm$). The uncertainty in static pressure was computed to be ± 70 Pascals. To note, at the lowest measured value of cavitation inception, this corresponded to less than 1 % error in static pressure measurement.

Tunnel Free Stream Velocity- U_∞ Tunnel freestream velocity is determined by a differential pressure cell located in the contraction section. To calibrate it, a velocity cut is taken (without the foil in the test section) along the z axis, at the center of the test section (in x and y). The velocity reading of the laser is compared with that of the dpcell, and the calibration constants are adjusted

accordingly. See Fig. C-1 for calibration curves. The combination of pre and post calibration drift and LDV uncertainty gives and uncertainty of U_∞ to be $\pm$ 0.05 m/s

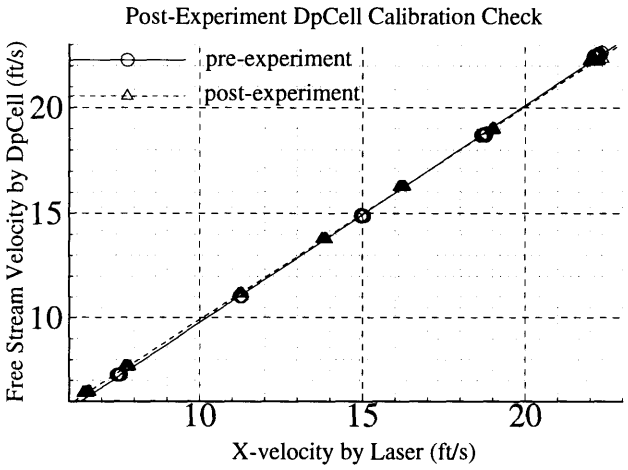

Figure C-1: DpCell calibration: pre-experimental values with calibration constants adjusted, and post-experiment values

Laser Position Laser position was measured by digital traverse/encoder system. The laser positioning system has a resolution of .001 mm and relative accuracy of better than 0.01mm . Thus for the purposes of error analysis, this position error was negligible. Even in the determination of angle of attack, observer reproduceability dominates the errors.

Other Measurements .. ..

Water Temperature : $\pm 0.25C$ (instrument accuracy)

P_{vap} : less than $\pm 100Pa$ (based on temperature error)

ρ : less than $\pm 0.1\%$ (based on temperature error and drift)

ν : less than $\pm 2.5\%$ (based on temperature error and drift)

P_{base}: less than $\pm 15Pa$ (based on liquid column height and density errors)

Tunnel air content (undissolved): less than 1% by volume (see discussion in Procedure)

C.3 Computed Quantities

Reynolds Number The uncertainty ranges in reports of Reynolds number are derived from the drift in U_∞ and T in the course of the experiment:

$$\frac{\Delta \mathrm{Re}}{\mathrm{Re}} = \frac{\Delta T}{T} + \frac{\Delta U_\infty}{\overline{U}_\infty}, \tag{C.2}$$

Tested at Re=3ee6, \alpha =-0.5^o

Run #	File	Alpha	Cl	Cd
1	PT5R1	-0.508	0.1988	0.0103
2	PT5R1_4	-0.490	0.1927	0.0092
3	PT5R1_y	-0.543	0.1987	0.0104
4	PT5R1_A	-0.536	0.2035	0.0105
Mean Values:			0.1984	0.0101

R & R Error Results:

Cl range : +/- 0.0065

Cd range : +/- 0.001

Table C.1: Reliability and Reproducability Data for Lift and Drag coefficients by integrated contour method

where ΔT is the half the range over which the temperature varied in the course of the experiment, ΔU_∞ is half the drift range of the free stream velocity, and $\overline{U}_\infty$ is the mean free stream velocity. From this computation the error in Reynolds number was estimated at $\pm 5.0\%$ maximum.

Angle of Attack The stated error range for angle of attack, $\Delta\alpha$ represents the total angle shift from before and after test measurements combined with observer repeatability measurements using two different observers. This was measured to be 0.01 degrees in the worst case.

Other than observer repeatability, the other sources of error are related to the laser positioning device. With an accuracy of better than 0.01mm the error due to positioning tolerance is less than 0.0015 degrees.

Lift and Drag by Contour Integration Table C.1 shows the results of contour calculations on repeated measurements of the same test case. The result of these four results shows that the contour integration method is repeatable to about ± 0.0065 on Cl and ± 0.001 on Cd. Since the uncertainty in the individual measurements used in the contour integral is much smaller than these repeatability ranges, it is assumed that these uncertainties are captured in these repeatability ranges.

Cavitation Number at Inception Cavitation number uncertainty(statistical):

The equation to compute cavitation number is:

$$\sigma = \frac{P_{stat} - P_{vap}}{\frac{1}{2}\rho U_\infty^2}$$

Thus through first order statistical error analysis the estimated error becomes

$\%\delta\sigma = [(\%delP + \%delPvap)^2 + \%delrho^2 + 2 * \%delV^2]^{0.5}$.

From this relation the relative error in cavitation measurement is found to be $\pm 3.3\%$.

Of greater consequence to cavitation inception errors are the reliability and Repeatability of observed inception. This was determined to be less than ± 0.05 on σ at inception for the worst conditions over the course of the experiment from multiple inception observations by various observers. These observation error bars are plotted on cavitation bucket diagrams for cases where it was measured.

Appendix D

Foil Offsets

Table A1 - Parent Foil Offsets

OS 20 (10/20) 4.5 (70/85/97) 0.2

(Stations and Offsets in Percent of Chord)

X	Y-Upper	Y-Lower	Thickness	Camber
0.0000	0.0000	0.0000	0.0000	0.0000
0.1000	0.2076	-0.2036	0.4111	0.0020
0.2500	0.3375	-0.3274	0.6648	0.0050
0.5000	0.4911	-0.4709	0.9620	0.0101
1.0000	0.7200	-0.6793	1.3992	0.0204
1.5000	0.9036	-0.8420	1.7455	0.0308
2.5000	1.2061	-1.1017	2.3078	0.0522
3.5000	1.4599	-1.3111	2.7711	0.0744
5.0000	1.7865	-1.5681	3.3546	0.1092
7.5000	2.2406	-1.8969	4.1375	0.1719
10.0000	2.6204	-2.1374	4.7578	0.2415
12.5000	2.9474	-2.3054	5.2527	0.3210
15.0000	3.2329	-2.4077	5.6406	0.4126
17.5000	3.4841	-2.4512	5.9353	0.5165
20.0000	3.7059	-2.4436	6.1495	0.6311
25.0000	4.0736	-2.3204	6.3940	0.8766
30.0000	4.3546	-2.1093	6.4639	1.1227
35.0000	4.5599	-1.8500	6.4099	1.3549
40.0000	4.6962	-1.5697	6.2659	1.5633
45.0000	4.7677	-1.2882	6.0559	1.7397
50.0000	4.7760	-1.0205	5.7965	1.8777
55.0000	4.7207	-0.7780	5.4987	1.9714
60.0000	4.5990	-0.5685	5.1675	2.0152
65.0000	4.4037	-0.3968	4.8006	2.0034
70.0000	4.1199	-0.2631	4.3830	1.9284
72.5000	3.9327	-0.2076	4.1403	1.8626
75.0000	3.7072	-0.1574	3.8646	1.7749
77.5000	3.4427	-0.1126	3.5553	1.6650
80.0000	3.1405	-0.0734	3.2140	1.5336
82.5000	2.8036	-0.0405	2.8442	1.3815
85.0000	2.4371	-0.0150	2.4521	1.2111
87.5000	2.0515	0.0009	2.0506	1.0262
90.0000	1.6571	0.0049	1.6522	0.8310
92.5000	1.2588	-0.0030	1.2618	0.6279
95.0000	0.8599	-0.0225	0.8824	0.4187
96.5000	0.6225	-0.0397	0.6622	0.2914
97.5000	0.4671	-0.0537	0.5208	0.2067
98.5000	0.3166	-0.0703	0.3869	0.1231
99.0000	0.2433	-0.0797	0.3230	0.0818
99.5000	0.1713	-0.0896	0.2609	0.0408
100.0000	0.1000	-0.1000	0.2000	0.0000

Table A2 - Blunt Based Foil Offsets

OS 19.3 (86/10/20)1.4 5.7 (70/97/98)1.4 2.0

(Stations and Offsets in Percent of Chord)

X	Y-Upper	Y-Lower	Thickness	Camber
0.0000	0.0000	0.0000	0.0000	0.0000
0.1000	0.2226	-0.2198	0.4425	0.0014
0.2500	0.3602	-0.3531	0.7133	0.0035
0.5000	0.5215	-0.5073	1.0288	0.0071
1.0000	0.7597	-0.7311	1.4908	0.0143
1.5000	0.9492	-0.9059	1.8552	0.0217
2.5000	1.2594	-1.1857	2.4451	0.0369
3.5000	1.5180	-1.4125	2.9305	0.0528
5.0000	1.8489	-1.6930	3.5420	0.0779
7.5000	2.3066	-2.0587	4.3654	0.1239
10.0000	2.6881	-2.3359	5.0240	0.1761
12.5000	3.0160	-2.5425	5.5585	0.2367
15.0000	3.3023	-2.6867	5.9890	0.3078
17.5000	3.5547	-2.7757	6.3303	0.3895
20.0000	3.7780	-2.8170	6.5950	0.4805
25.0000	4.1512	-2.7969	6.9481	0.6671
30.0000	4.4414	-2.6902	7.1316	0.8756
35.0000	4.6605	-2.5326	7.1931	1.0639
40.0000	4.8163	-2.3484	7.1646	1.2339
45.0000	4.9138	-2.1553	7.0691	1.3793
50.0000	4.9565	-1.9667	6.9231	1.4949
55.0000	4.9458	-1.7926	6.7384	1.5766
60.0000	4.8821	-1.6403	6.5225	1.6209
65.0000	4.7638	-1.5142	6.2780	1.6248
70.0000	4.5859	-1.4148	6.0008	1.5855
72.5000	4.4698	-1.3732	5.8431	1.5483
75.0000	4.3337	-1.3356	5.6693	1.4991
77.5000	4.1779	-1.3018	5.4796	1.4380
80.0000	4.0007	-1.2716	5.2723	1.3646
82.5000	3.7985	-1.2442	5.0427	1.2772
85.0000	3.5652	-1.2183	4.7836	1.1734
87.5000	3.2925	-1.1922	4.4847	1.0501
90.0000	2.9702	-1.1637	4.1338	0.9032
92.5000	2.5868	-1.1304	3.7173	0.7282
95.0000	2.1314	-1.0906	3.2220	0.5204
96.5000	1.8202	-1.0634	2.8836	0.3784
97.5000	1.5971	-1.0443	2.6414	0.2764
98.5000	1.3636	-1.0253	2.3889	0.1691
99.0000	1.2442	-1.0165	2.2607	0.1139
99.5000	1.1232	-1.0081	2.1312	0.0575
100.0000	1.0000	-1.0000	2.0000	0.0000

Bibliography

[1] I. H. Abbott and A. E. Von Doenhoff. *Theory of Wing Sections.* Dover, New York, 1959.

[2] F. S. Archibald. Self-Excitation of an Acoustic Resonance by Vortex Shedding. *Journal of Sound and Vibration*, 38(1), 1975.

[3] O. Scherer B. Cox, R. Kimball. Hydrofoils Sections With Thick Trailing Edges. SNAME Propellers/Shafting, September 1997.

[4] R. Eppler and Y. T. Shen. Wing Section for Hydrofoils - Part 1: Symmetric Profiles. *Journal of Ship Research*, 23(3), 1979.

[5] R. Eppler and Y. T. Shen. Wing Section for Hydrofoils - Part 2: Non-symmetrical Profiles. *Journal of Ship Research*, 25(3), 1981.

[6] Spyros A. Kinnas. Hydrofoil Lift and Drag From Momentum Integrations. Technical Report Rep. 91-4, Department of Ocean Engineering, Massachusetts Institute of Technology, November 1991.

[7] E. H. Lurie. Unsteady response of a two-dimensional hydrofoil subjected to high reduced frequency gust loading. Master's thesis, Massachusetts Institute of Technology, 1993.

[8] J. N. Newman. *Marine Hydrodynamics.* MIT Press, 1977.

[9] D. E. Egnor R. W. Kimball. HRA 2D Foil Experiment. Technical Report Rep. 97-2, Department of Ocean Engineering, Massachusetts Institute of Technology, May 1997.

[10] Y. T. Shen. Wing Section for Hydrofoils - Part 3: Experimental Verification. *Journal of Ship Research*, 29(1), 1985.